
Surface and Coatings Technology
Q1
Chemistry (miscellaneous)
best quartile
SJR 2021
0.92
powered by scimagojr.com

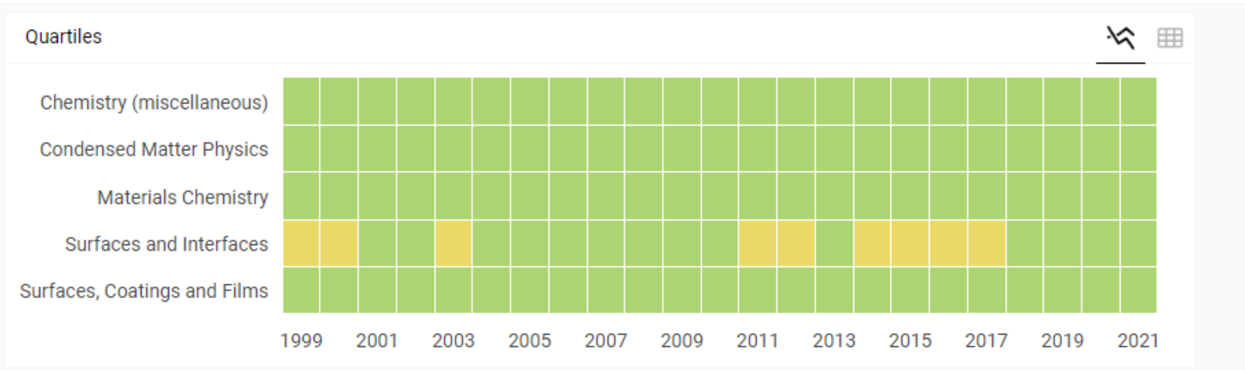
Quartiles
Chemistry (miscellaneous)
Condensed Matter Physics
Materials Chemistry
Surfaces and Interfaces
Surfaces, Coatings and Films
1999
2001
2003
2005
2007
2009
2011
2013
2015
2017
2019
2021

Surface & Coatings Technology 434 (2022) 128226

Contents lists available at ScienceDirect

Surface & Coatings Technology

journal homepage: www.elsevier.com/locate/surfcoat

Full length article

Ultrafast microstructure modification by pulsed electron beam to enhance surface performance

Yanfei Geng [a,b,c], Xizhang Chen [a,b], Sergey Konovalov [a,b,c,*,**], Irina Panchenko [b], Yurii Ivanov [d], Vladislav Deev [e,f], Evgeny Prusov [g]

[a] Institute of Laser and Optoelectronic Intelligent Manufacturing, Wenzhou University, Wenzhou, China
[b] Siberian State Industrial University, Novokuznetsk, Russia
[c] Samara National Research University, Samara, Russia
[d] Institute of High Current Electronics, Siberian Branch, Russian Academy of Sciences, Tomsk, Russia
[e] Department of Metal Forming, National University of Science and Technology MISiS, Moscow, Russia
[f] School of Mechanical Engineering and Automation, Wuhan Textile University, Wuhan, China
[g] Department of Functional and Constructional Materials Technology, Vladimir State University, Vladimir, Russia

ARTICLE INFO

Keywords:
Electron beam energy density
Al-Mg alloy
Subgrain
Phase composition
Nano-hardness
Friction coefficient

ABSTRACT

Pulsed electron beam surface treatment was used to enhance the microstructure and surface mechanical properties. After treatments with different electron beam energy densities, the microstructure and nano-structure of additively manufactured Al-Mg alloys were evaluated by scanning and transmission electron microscopy. At high E_s (15 J/cm^2) treatment, there is around 30–35 μm melting layer and the new second phase with complex elemental composition ($Mn_{4.6}Fe_{0.4}Si_3$) in the surface modification layer. Thermal stress within different E_s has a different effect on the second phase and dislocations, and the thermal stress in high E_s improves the dissolution of submicron-sized inclusions presented in the initial state to form new particles. KAM (Kernel Average Misorientation) maps and calculated values prove that the electron beam irradiation increases the degree of local misorientation and surface stress. As E_s is up to 15 J/cm^2, the value of KAM and stress, as well as the dislocation, is the maximum. The formation of subgrains and precipitates with complex elemental composition after irradiation has comprehensive effects on the nano-hardness, wear rate and friction coefficient. It reveals that the nano-hardness and the friction coefficient of samples irradiated by 15 J/cm^2 have the highest and the lowest values, respectively.

1. Introduction

5xxx aluminum alloys process high strength, excellent corrosion resistance, low densities and good formability [1–2]. Due to those advantages, it is considered to be an appropriate choice for vehicle structures, such as wheels, chassis and sub-frames [3]. Among the manufacturing methods for Al-Mg alloys, the technology of wire arc additive manufacture (WAAM) has garnered widespread attention as the most promising and economical method [4–5]. At present, there are still some problems during processing. The grain size is generally large (columnar grains) and there are visible pores along grain boundaries, which are demonstrated in the literature [6–7]. Due to the complicated thermal cycle during the manufacturing process, the microstructure morphology of each deposited layer is different and coarse columnar grains and fine equiaxed grains are non-uniformly distributed [8]. Except that, it was found that the distribution of different elements in those zones was not homogeneous, while the treatment can improve this phenomenon [9]. The Mg is the second main element in Al-Mg alloys, and the Mg forming solid solution is contributed to the serrated yielding performance [10]. Besides, the Mg-rich secondary β phase can help increase dissolution along the grain boundaries and exfoliation of entire grains into solution in corrosion experiments [11]. During the process, the loss of elemental Mg has a strong effect on the tensile strength and average hardness because of non-uniform distribution in different zones

* Corresponding author at: Institute of Laser and Optoelectronic Intelligent Manufacturing, Wenzhou University, Ocean Science and Technology Innovation Park, No. 19 Binhai 3rd Road, Yongxing Street, Longwan District, Wenzhou, Zhejiang 325024, China.
** Corresponding author at: Samara National Research University, 34, Moskovskoye Shosse, Samara 443086, Russia.
E-mail address: ksv@ssau.ru (S. Konovalov).

https://doi.org/10.1016/j.surfcoat.2022.128226
Received 8 October 2021; Received in revised form 4 February 2022; Accepted 5 February 2022
Available online 10 February 2022

[4]. It is known that the main phases in the Al-Mg alloy manufactured by wire and arc additive manufacturing based on cold metal transfer technology include the α phase (Al) and β phase (Al_3Mg_2) [6]. β phase was reported to nucleate and grow intragranularly along α grain boundaries [12]. The nanostructure and phase composition is dominated by the distribution of the elements and temperature gradient during the multi-layer melting processing. The hardness and wear resistance is influenced by inhomogeneous phase composition and precipitates distribution [13]. The differences in microstructure morphology and phase composition, as well as the nanostructure, contribute to the change in mechanical properties. The microstructure and mechanical properties of the parts manufactured by WAAM-CMT technology are intolerable for engineering applications, especially the surface [9]. To enhance the surface properties of WAAM-CMTed Al alloy parts, surface modification technologies of coating and energy beams such as ion, electron, laser, and plasma are proposed [14–18].

As worthy noticed, the electron beam is particularly applied to enhance surface properties and microstructure due to extremely high instantaneous energy density, short irradiation time and high surface finishing without any change in the substrate materials [19–20]. The whole process is developed in a vacuum environment as well [21]. Considering the techniques of electron beam surface treatment improving the overall properties and behavior of materials, it has become a feasible and effective method. Hence, the researchers pay more attention to electron beam surface treatment for improving surface properties and microstructure [22–23]. About the condition of high heat input during the treatment process, the melting phenomenon of the surface layer happened so that the alloying elements were going to redistribute [24]. 'Melting mode' and 'heating mode' were stated to distinguish the high and low heat input on the surface. It was demonstrated that the formation of a homogeneous layer was obtained in melting mode and heavy deformation induced in the heating mode made texture modification [25–26]. The significant changes in the microstructure morphology and distribution of elements were confirmed in the investigation of the electron beam surface rapid solidification of 2024 Al alloy [27]. After high current pulsed electron beam (HCPEB) treatment, vacancy and dislocations were significantly increased near the surface of aluminum specimens and the values of microhardness were higher than that of the heat-affected zone [28]. The effect of different currents and pulses on aluminum alloys was investigated and the results indicated that it had the proper microstructure and element distribution at the condition of 15-pulse and current 10^2–10^3 A/cm^2 [29]. With a similar value of pulse and current, energy density was set to the value of 2.5 J/cm^2, and the results showed the wear resistance and hardness indeed increased due to the redistribution of strengthening elements [30]. With the parameters of 1 and 5 pulses at about 1 J/cm^2, the deformation twins and a large number of small vacancy clusters without dislocations were found in the near-surface of the aluminum single crystal [31]. Comparatively, Samih et al. found the existence of large grains, up to 50 μm in diameter, at the surface of an AISI420 martensitic stainless steel [32] and Yan et al. also found a similar phenomenon in 2024 alloys after HCPEB processing [33]. With the increase of energy density (4.5 J/cm^2) and pulse number (30), the aluminum coating irradiated by HCPEB presented densification texture, high hardness and outstanding anti-crrosion performance [34]. In the studies of different energy densities, it revealed that the maximal microhardness value was at the condition of E_s = (30–40) J/cm^2, but the analysis of the effect of energy density on element distribution was not stated [35]. The investigation of pulse numbers for 2024 Al alloys demonstrated that the samples irradiated by 24 pluses HCPEB showed the best corrosion properties but the hardness of the sample at 6 pulses was the highest value (155 HV) [36]. As for the nano-structure, some reports stated that the vacancy cluster defects including dislocation loop stacking fault tetrahedra and void were observed in aluminum alloys after HCPEB treatments [31]. It was pointed out that texture development could be influenced during the solidification process and the fiber texture was formed on the materials after a sufficient number of pulses [27,37]. While continuous and uniform crater-like cavities were found on the surface layer and their presence promoted the formation of the high-quality textured surface [38]. The number of investigations highlighted that the different electron beam surface treatments (different pulses, currents and energy densities) could refine grain size and improve mechanical properties [21–22,39]. The effect of the electron beam on aluminum alloys is controversial, although the technique of electron beam treatment is considered to be the most promising surface modification method. Additionally, there are few reports and investigations about the modification of additively manufactured Al-Mg alloys by electron beam processing. Investigations of electron beam treatment applied on the additively manufactured Al-Mg alloy are significant for the promotion of wire arc additive manufactured aluminum alloys.

In order to investigate the effect of different electron beam energy densities on the phase composition and element distribution, this paper presents detailed transmission electron microscopy (TEM) and scanning electron microscopy studies of the modification layer and second phases. Electron backscatter diffraction (EBSD) is used to investigate the condition of the local misorientation and the stress on the surface layer. As well, the measurement of nano-hardness and wear properties is performed to study the relationship between mechanical properties and electron beam energy densities.

2. Material and methods

2.1. Al-Mg alloys manufactured by WAAM-CMT

The target sample was constructed by wire arc additive manufacture (WAAM), equipped with a cold metal transfer (CMT) system. The system of WAAM-CMT includes a Fronius CMT-Advance power source, a wire feeder, the robot controller, and the CMT torch connecting with the six-axis Fanuc robot. To deposit the specimen, 1.2 mm diameter filler wire (ER 5356) was used. The multilayer deposition was developed on the substrate which is a 6061-T6 aluminum alloy plate with the dimension of 200 × 60 × 10 mm^3. The composition of ER 5356 filler wire is shown in Table 1. To manufacture the desired sample, the current and voltage were set at 168 A and 19.9 V, and the wire feed and travel speed were set at 7.5 m/min and 0.6 m/min, respectively. In the whole manufacturing process, 99.99% argon was employed as the shielding gas. The distance between the nozzle and the workpiece was set at 15 mm.

2.2. Pulsed electron beam surface treatments

Polished samples of additively manufactured Al-Mg alloy with 20 × 15 × 10 mm^3 dimensions were used. The pulsed electron beam surface treatment was carried out on the SOLO equipment (Institute of High Current Electronics, Tomsk, Russia). The SOLO equipment could provide a rather intense energy density compared to other HCPEB machines (e.g. the HOPE used in China). This equipment effectively modified the mechanisms of microstructure and surface properties which were discussed in several papers [23,36,40–42]. The treatment of electron beam processing with the same pulse number for the surface layer of aluminum alloys can be named pulsed electron beam surface treatment. The abbreviation of this technology is PEBST. The schematic diagram of the SOLO equipment is shown in Fig. 1. Three different electron beam energy densities (E_s = 5, 10, and 15 J/cm^2) were adopted in this experiment. Accelerate voltage was set at 18 kV, and pulse duration and the number of pulses were set at 200 μs and 3 respectively. The different

Table 1
The chemical composition of ER 5356 filler wire (wt%).

Alloy	Mg	Mn	Fe	Cu	Si	Al
ER 5356	4.5–5.5	0.2–0.25	0.4	0.1	0.25	Bal.

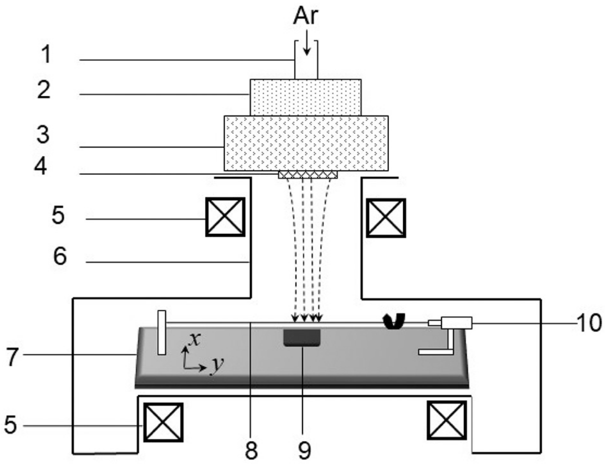

Fig. 1. Working principle diagram of the electron beam processing equipment (SOLO): 1-hollow anode of the ignition discharge; 2-hollow cathode; 3-hollow node of the main discharge; 4-emission grid; 5-coils; 6-drift tube; 7-the x-y coordinate manipulator; 8-treated spoke; 9-specimen; 10-electric motor rotating the spoke.

PEBSTs were developed in the vacuum chamber with residual gas (Ar, 0.02 Pa).

2.3. Microstructure and mechanical properties

After erosion, the cross-sections of all samples with the size 10 × 10 × 20 mm^3 were observed on the TESCAN VEGA scanning electron microscope (SEM: Oxford Instruments, Britain). The precipitates and dislocations were analyzed by transmission electron microscope (TEM). The position of TEM observation samples is shown in Fig. 2. Thin foils were cut from the cross-section which is perpendicular to the surface, from the surface to 1 mm in depth. The TEM samples were mechanically thinned to around 50 μm by the Ion Slicer EM-09100IS. The TEM experiments were carried out on the JEM-2100F JEOL equipment (JEOL Ltd. Tokyo, Japan). The electropolished solution concludes nitric acid (33 vol%) and methanol (67 vol%). All samples for TEM analysis were electropolished at the temperature of 253 K and the current was set to 12 A.

The electron backscatter diffraction (EBSD) measurements were carried out using a scanning electron microscope (SEM; SUPRA55, Carl Zeiss, Germany). The samples for EBSD analysis were cut from the modification layer, as shown in Fig. 2. All data generated from those experiments were analyzed with the help of HKL Channel 5 and JTEX software analysis system [43]. The tolerance angle of the exact orientation was set to 10°.

The nano-hardness of the micro-zone has been detected by the constant displacement method, and the dentation depth is kept at 1000 nm. Nanoindentation measurements were performed using a MTS nanoindenter DSM tester (MTS, America).

Tribological properties (wear resistance and friction factor) were determined on planar samples using tribometer Pin–On–Disc and Oscillating TRIBOtester (TRIBOTechnic, France) with the following parameters: 6 mm diameter ball made of Al_2O_3 ceramic material, the sample rotation rate of 25 mm/s, the path traveled by counter-body of 100 mm, indenter load of 5 N, wear track radius of 2 mm, at room temperature and normal humidity. The coefficient of friction was measured continuously during the test period and the data were collected on a computer. To calculate the wear rate, the formula was used in this experiment is presented in Eq. (2.1)

$$K = \frac{2\pi RA}{FL} \tag{2.1}$$

where R – a radius of wear track; A – a cross-section of wear groove; F – is the normal load applied to the disk; L– is the sliding distance.

3. Simulation of temperature on the surface

In numerous works performed on samples of various metals and alloys, it is shown that irradiation of a solid body by a pulsed electron beam allows modification of the defective substructure and phase composition of the surface layer [44–46]. The structure and thickness of the modified layer are determined by the type of irradiated material (metal, alloys, metal-ceramic and ceramic materials) and the irradiation mode.

The alloy irradiation mode is chosen based on the results of modeling the temperature field formed in the material during the process of pulsed electron beam irradiation. With the application of the finite difference method, the thermal conductivity equation is used to find the temperature field in a certain range of the electron beam energy density. Therefore, the calculations for electron beam energy densities with two kinds of pulse duration (50 and 200 μs) were performed, the range of E_s from 5 J/cm^2 to 30 J/cm^2.

The relationship between electron beam energy density and surface temperature can be described by the Eq. (3.1) [47]:

$$\mathrm{L}_v(x,t) = \frac{E(t)E_0(t)}{r(t)e} f(x,r) \tag{3.1}$$

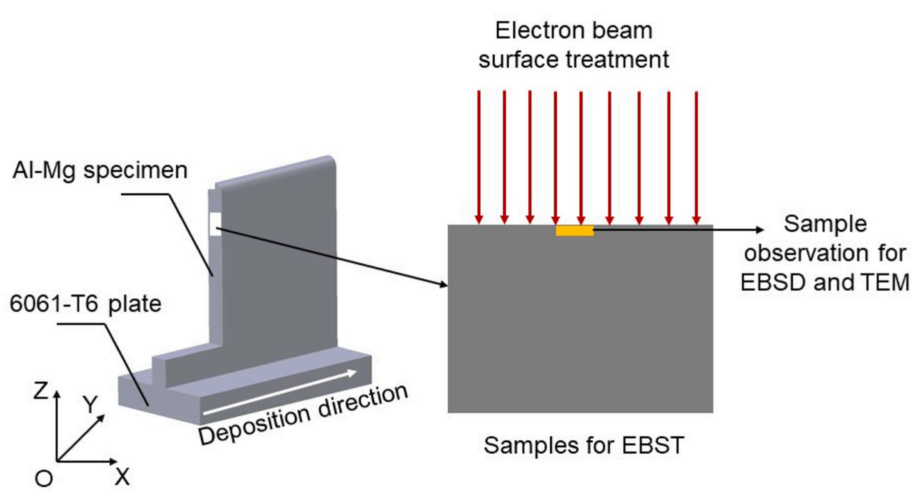

Fig. 2. The diagrammatic of sample observation for EBSD and TEM.

where $E(t)$ is the electron current density in this paper; $E_0(t)$ is the initial electron energy, e is the electron charge, $r(t)$ is the electron range in the target, and $f(x,y)$ is the distribution function of the electron beam losses in depth. The function $f(x,y)$ is the third-degree polynomial, as shown in Eq. (3.2) [47–48]:

$$f(x,r) = 0.74 + 4.7xr^{-1} - 8.9\left(xr^{-1}\right)^2 + 3.5\left(xr^{-1}\right),\quad x \in [0; r]. \tag{3.2}$$

The electron range was established by the Eq. (3.3):

$$r(E_0) = C(E_0/e)^{3/2}\Big/\rho \tag{3.3}$$

where C is a constant equal to 10^{-4} kg/($m^2V^{3/2}$) and E_0 is measured in kiloelectron-volts.

The thickness of the surface layer for thermal calculations was taken equal to $0.5 \cdot 10^{-3}$ m, the observation time was 600 μs. The thermophysical values of aluminum used in this calculation are shown as follows: thermal conductivity coefficient k = 93 W/(m·K), specific heat capacity $c_p = 1177 \cdot 10^{-3}$ J/(g·K), density ρ = 2.69 g/cm^3, melting temperature T_{mp} = 933 K, evaporation temperature T_{eva} = 2793 K, melting heat q_m = 400 kJ/kg, heat of evaporation q_{eva} = 10,859 kJ/kg. Results of the simulation are shown in Fig. 3.

Fig. 3 shows the results of the simulation of the temperature changes with the electron beam energy density. The dotted lines indicate the values of electron beam energy density corresponding to different stages of material modification. It demonstrates the maximum temperature of aluminum surface heating increases as the electron beam energy density increases and the duration of the pulse exposure to the beam decreases.

4. Results

4.1. Cross-section microstructure of electron beam irradiated samples

A surface structure of additively manufactured Al-Mg alloy samples processed by the pulsed electron beam was analyzed by the SEM. Fig. 4 shows the cross-section structure of the etched section of additively manufactured Al-Mg alloy after different PEBSTs. The melting phenomenon and differences in microstructure are not found in Fig. 4(a) which was irradiated at the lower electron beam energy density (E_s = 5 J/cm^2). As defined, this condition without melting and phase transformation is called "Heating mode" [49]. In heating mode, the microstructure morphology of the modification layer is consistent with the matrix. As analyzed in previous studies, the main phase includes the

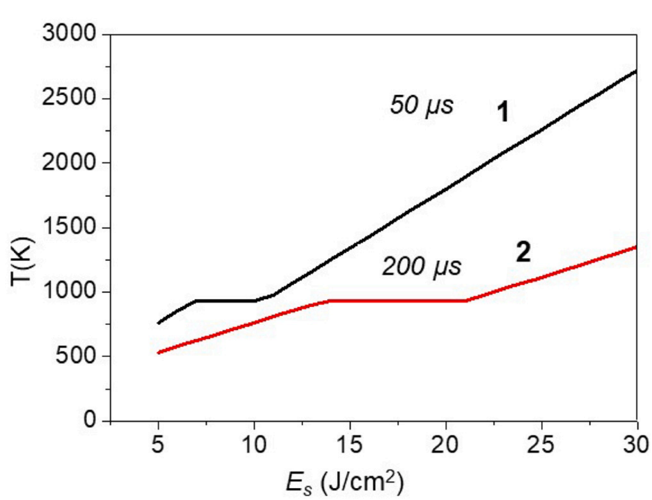

Fig. 3. Dependence of the maximum temperature on the surface of the aluminum sample with the electron beam energy density at exposure times of 50 μs (curve 1) and 200 μs (curve 2).

α-phase (Al) and β-phase (Al_3Mg_2) and the black particles are found along the grain boundaries or scatter in the grain [6]. The black dots consist of Al and Mg which is considered to be Al_3Mg_2. With the E_s increasing to 10 J/cm^2, there is also no difference in matrix metal, but the surface layer is different from the one in 5 J/cm^2, which is seen in Fig. 4(b). The remelting phenomenon is also difficult to be found in this condition. Based on the phenomenon at this condition, when the E_s is 10 J/cm^2, the treated surface is also in the "heating mode". As increasing to 15 J/cm^2, there are two visible boundary lines located in the surface area, as observed in Fig. 4(c). The remelted layer, heat-affected zone (HAZ) and matrix are separated by those two lines, and the modification layer includes remelted layer and HZA which can be seen in Fig. 4(d). A similar phenomenon was observed in the N18 samples treated by 25-pulsed electron beam surface treatment [46]. In this condition, there is a melting phenomenon observed on the surface, therefore, it is named as the surface is in the "melting mode" based on the definition [49]. In "melting mode", the surface layer suffered super-fast melting at high-temperature treatment and super-fast cooling to room temperature in the vacuum chamber. After 15 J/cm^2 of electron beam irradiation, there are some microcracks from the surface extending to the Al matrix along grain boundaries, as seen in Fig. 4(d). With the comparison of remelting layer and HAZ, there are more black particles in the HAZ. The size of particles is bigger than the one distributed in the matrix and remelting layer. Except that, along the boundary line between HZA and remelting layer, there are many second phase particles along this line. Meanwhile, with the loss of elemental Mg caused by the increasing E_s the intergranular cracks were extended which was demonstrated in the previous study [50]. As is usually the case for electron beam irradiated samples testing, the differences in microstructure in surface and cross-sections are dominated by differences in E_s to initiate phase transition.

4.2. Kernel average misorientation of electron beam irradiated samples

The pulsed electron beam surface treatment has the characteristics of super-fast heating and cooling speed. Under the high-temperature cycle, the surface stress distribution and grain morphology of samples will make a difference. It is difficult to see the differences in SEM images. The EBSD is the appropriate method to have a further investigation on the modification layer. Kernel Average Misorientation (KAM) is proposed by Wright [51] and has been widely used in EBSD mapping for indicating the dislocations density through quantifying local distortion of crystalline materials [52]. In this study, the KAM maps have been developed to visualize local misorientations. The EBSD measurement results are shown in Fig. 5, it shows the KAM maps measured from specimens untreated as well as treated in different electron beam irradiations. KAM maps are all scaled to a minimum of 0° represented by blue and a maximum of 5° represented by red. Here, the average misorientation of an EBSD point is calculated with respect to all neighbors at a 500 nm distance (values above 2° are excluded). The areas surrounded by the black lines represent grains. Without PEBST irradiation, the high KAM value distribution is mainly presented in few grains, which is shown in Fig. 5(a). As the E_s increasing, the distribution of high KAM values inside grains is increasing and some small subgrains are observed, as seen in Fig. 5(b)–(d).

The KAM maps of PEBST irradiated specimens reveal that the high E_s (15 J/cm^2) increases the KAM value and high degree of local misorientation. The KAM maps reveal areas with an increased density of the dislocations and may reflect the material strain history [53]. With the comparation of KAM value distribution in different irradiations, the high KAM value caused by the increasing of electron beam energy density reveals the high stress in grains of the surface layer. It means that there is high-density dislocation distributed in the areas with high KAM values. When the E_s is 5 J/cm^2, the KAM value in grains is markedly increased due to the low energy and superfast irradiation, but there is no effect on the grain size and melting (Fig. 5(b)). The results of KAM maps prove the accuracy of the TEM analysis. In order to further investigate the effect of

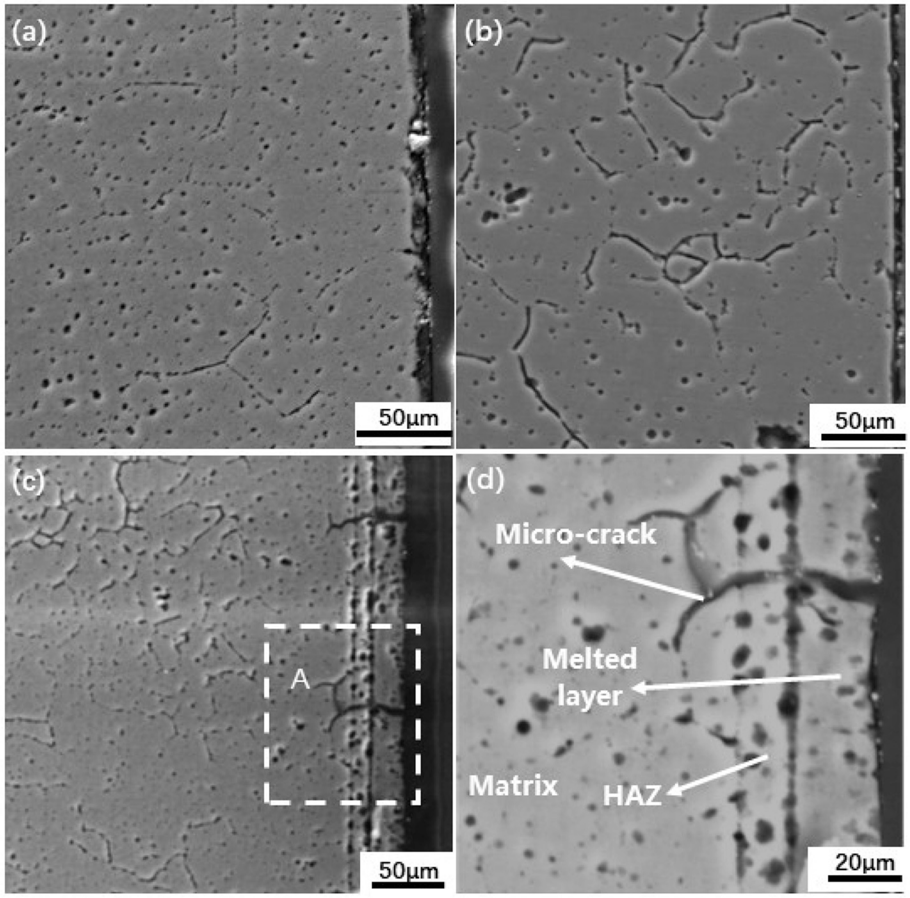

Fig. 4. SEM cross-section micrograph of additively manufactured Al-Mg alloy after different electron beam energy densities: (a) $E_s = 5$ J/cm^2, (b) $E_s = 10$ J/cm^2, (c) $E_s = 15$ J/cm^2 and (d) the magnified marked part (A) of (c).

electron beam energy density on structure, the frequency of local misorientation is needed.

The KAM is associated with a misorientation of less than 5°. Therefore, the KAM histogram was used to assess the local plastic strain in PEBST irradiated Al-Mg specimens. Fig. 6 gives the frequency distribution histograms of KAM values measured from the non-irradiated specimen as well as the specimen irradiated with different E_s. The observations of the frequency in local misorientation distribution histograms reveal that the peak frequency and its related degree of local misorientation are decreased and increased, respectively, as the E_s increase. The degree of local misorientation in peak point is higher, thus the value of stress distribution on the surface layer is higher.

4.3. TEM analysis

The phase composition of additively manufactured Al-Mg alloys irradiated by different PEBSTs can not be analyzed by SEM. The SEM analysis provides macroscopic differences. To furtherly investigate the differences of the structure after different PEBSTs, TEM and selected area electron diffraction (SAED) is good to observe the types and morphology of second- phases. Fig. 7 shows bright-field TEM images of the additively manufactured Al-Mg samples before PEBST irradiation, it demonstrates the Al-Mg alloy belongs to the polycrystalline aggregate and the dislocation substructure in the form of chaotically distributed dislocations is observed in grains. Fig. 7(a) shows that there are two precipitations with hundreds of nanometers distributed along the grain boundaries. The elemental composition of those two precipitations was analyzed by micro X-ray diffraction, as seen in Fig. 7(c). It reveals that the precipitation with black color and irregular shape are made up of Fe and O, another precipitation with inconspicuous boundary and a color similar to the matrix consists of Mg. The Mg distribution (purple spots) along grain boundaries is higher than the α-Al matrix. Obviously, the detected inclusions will be the centers of grain-boundary crack nucleation. It will reduce the mechanical properties of the material. The precipitations distinguished from the matrix are also found in the grain which is observed in Fig. 7(b). As noticed, the precipitation is connected with the end of fuzzy boundary accompanied by the high-density dislocation. The precipitations could be considered as the second phases distributed in the grains and along grain boundaries.

TEM investigations of pulsed electron beam treated Al-Mg alloys with different E_s are shown in Figs. 8, 9 and 10. Compared to Fig. 7(a) and (b), some particles with deep color which are different from the basic phase were found in Figs. 8, 9 and 10. Those different particles with a size of 120 or 200 nm are considered as the precipitates (second phases), as the diffraction analysis in Fig. 7(c).

Analysis of the surface layer of additively manufactured Al-Mg alloy irradiated by a pulsed electron beam at $E_s = 5$ J/cm^2 reveals the formation of subgrain structure in the surface layer, as shown in Fig. 8. The size of the subgrain structure is around 120 nm, as shown in Fig. 8(a). The SAED pattern of the circular area in Fig. 8(a) is shown in Fig. 8(b). The ring pattern formed in the SAED image states the polycrystalline nature of this material and the microstructure consists of high angle grain boundaries. Along grain boundaries, high dislocation density is founded in Fig. 8(c) and it is higher than the sample before irradiation. Except that, the high dislocation density is also found in the grains, as observed in Fig. 8(d). It revealed that the E_s at 5 J/cm^2 has little effect on the change of phase constitution but facilitates the formation of high dislocation density. Dong et al. found that the thermal stress wave could

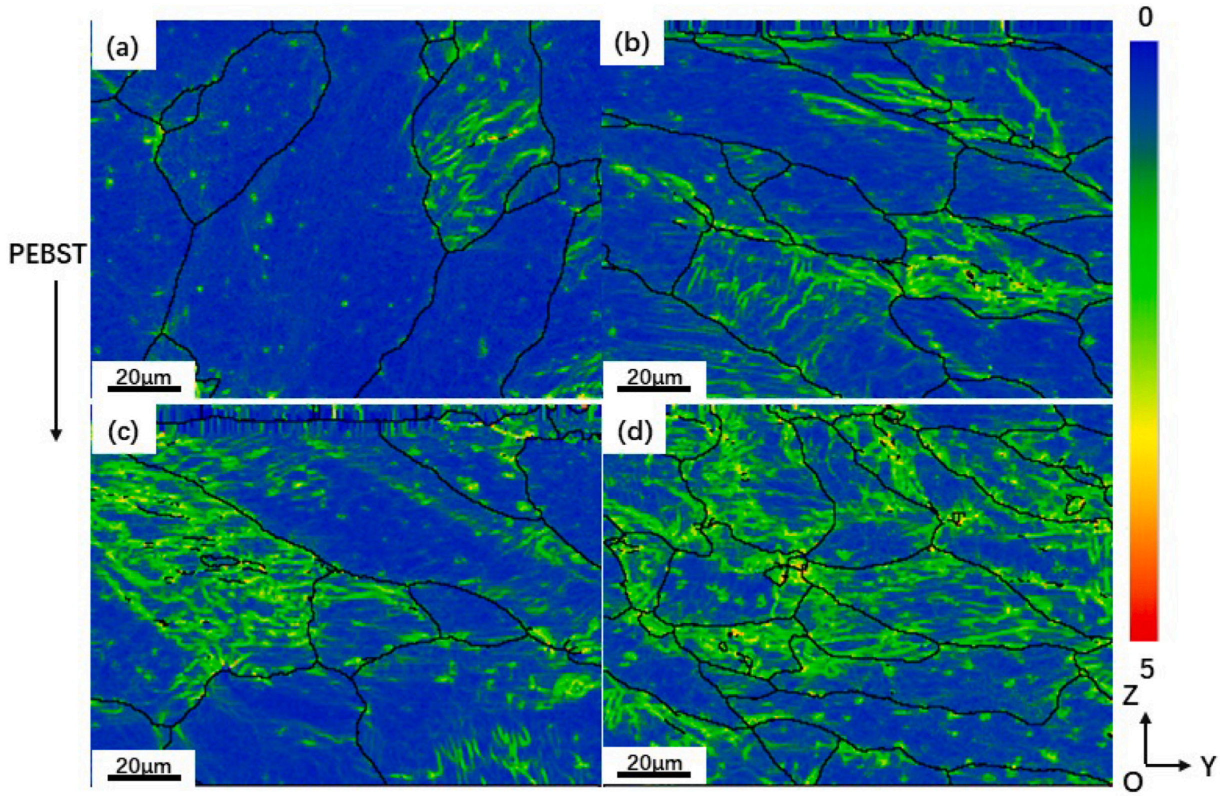

Fig. 5. KAM maps measured by EBSD of additively manufactured Al-Mg alloy after irradiation at (a) $E_s = 0$ J/cm^2, (b) $E_s = 5$ J/cm^2, (c) $E_s = 10$ J/cm^2 and (d) $E_s = 15$ J/cm^2.

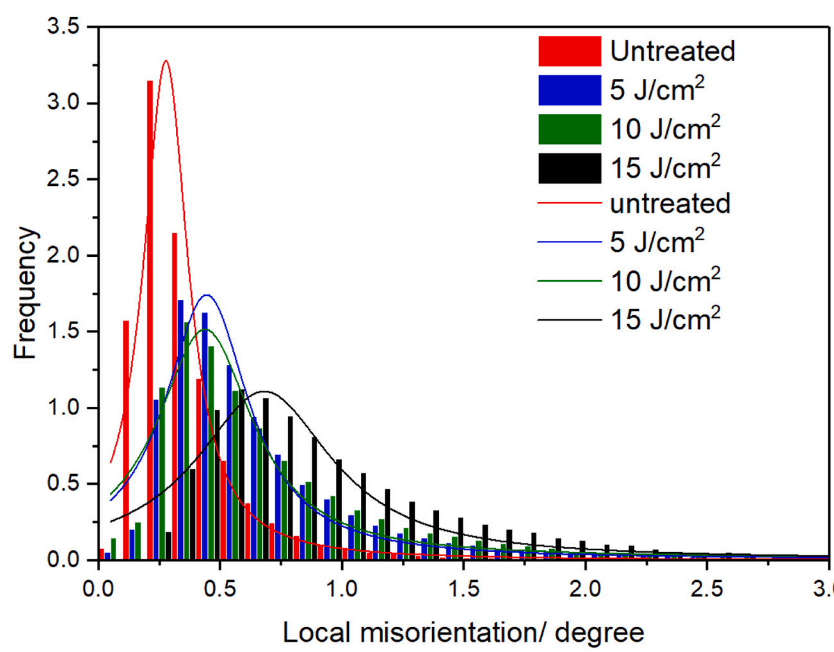

Fig. 6. Frequency distribution of local misorientation values measured from specimens irradiated by different electron beam energy densities.

be generated after irritation in aluminum alloys and the dislocations along the boundaries [54]. The results in this experiment are similar to the previous study.

Fig. 9 shows the TEM structure images of additively manufactured Al-Mg alloys after irradiation at $E_s = 10$ J/cm^2. As observed in Fig. 9(a), the number of subgrains is increasing and the sizes of subgrains increase from 120 nm to 200 nm. In the dark-field image (Fig. 9(b)), there are some precipitations formed in the subgrains and there are some dislocation lines distributed in the subgrains. There are some diffraction rings and symmetrically distributed diffraction spots. It proves that the formation of precipitations, thereupon the number of precipitations is increasing.

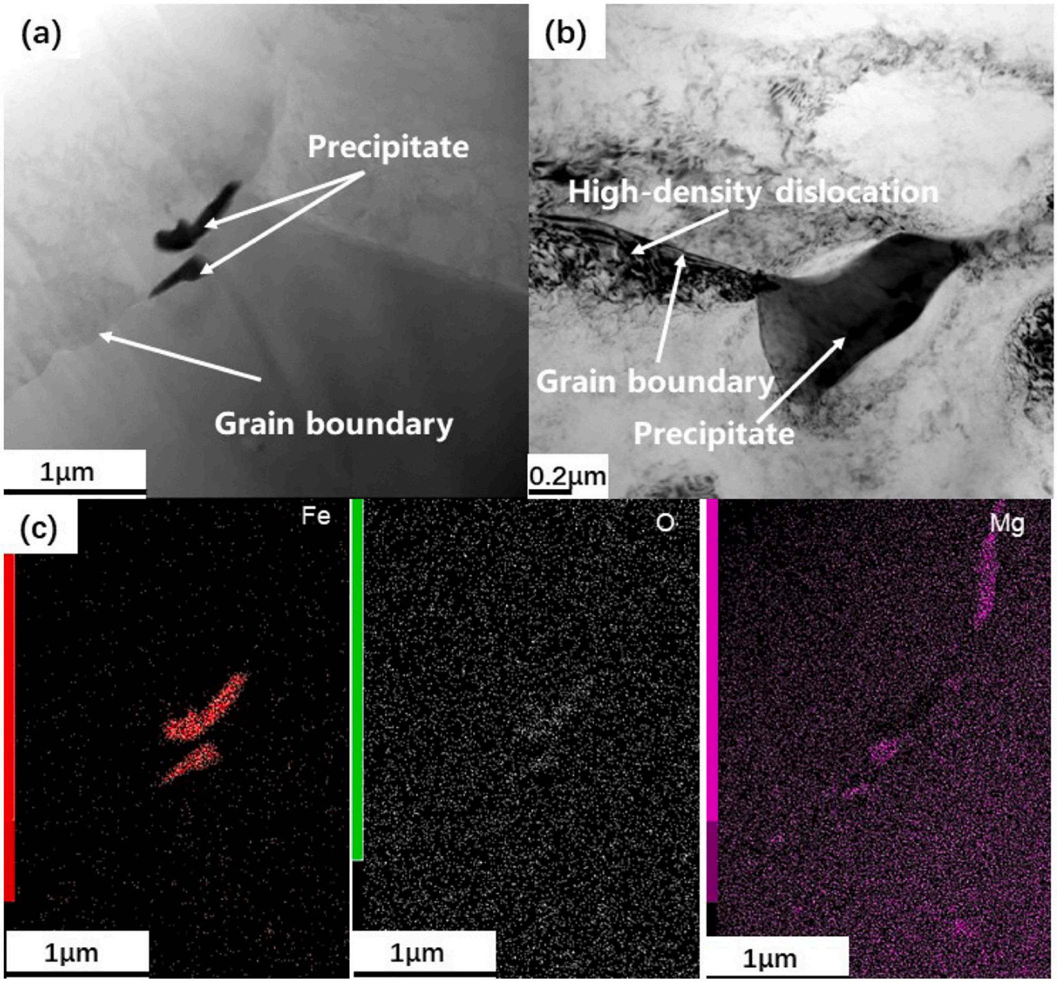

Fig. 7. Second phase distribution in the additively manufactured Al-Mg without electron beam processing: (a) the second phase located in the grain boundaries, (b) the morphology of the second phase, (c) EDX-TEM elements mapping of the binary eutectic obtained for Fig. 3(a) including Fe, O, and Mg.

Additively manufactured Al-Mg alloy treated by the pulsed electron beam in "melting mode" with the high energy beam density is accompanied by the formation of high-speed cellular crystallization (as shown in Fig. 10). In Fig. 10(a), there are dislocation tangles formed in the grains due to stress waves caused by the melting phenomenon during the high-temperature processing. The SAED pattern of the bright-field image in Fig. 10(b) demonstrates that the existence of precipitations ($Mn_{4.6}Fe_{0.4}Si_3$) and Al phase. Fig. 10(c) provides evidence for the formation of the precipitations with a size range from 10 to 13 nm. Additionally, the subgrains with a size varying from 350 to 500 nm could be observed in this dark-field image (Fig. 10(c)). As seen in Fig. 10(d), there are many waves formed in the Al matrix. With the energy density of the electron beam up to 15 J/cm^2, the surface layer of the sample suffered the high-temperature melting process. The stress state during the heating and cooling process is different. In this condition, the variation of stresses contributes to the formation of wave-lines or dislocation tangles. Therefore, the density of dislocations is increasing due to the formation of different dislocation tangles, as seen in Fig. 10(d). This result is consistent with the analysis of KAM.

4.4. Mechanical properties

The influence of processing parameters (E_s) on the average coefficient friction of EB irradiated AM Al-Mg alloys and the nano-hardness of different surface layers are shown in Fig. 11. For the comparison, the average coefficient of the untreated alloy is also included. The average friction coefficient of the four samples is different, which is observed in Fig. 11(a). As seen in the tendency of nano-hardness in Fig. 11(b), different nano-hardness values exhibited a direct influence on the wear behavior of the tested samples. As the nano-hardness increased the average coefficient was decreased. The wear rate determined according to the volume of the loss material is presented in Table 2. The pulsed electron beam irradiation indeed decreased the wear rate.

The differences observed in the evolution of the average friction coefficient and nano-hardness are dominated by the electron beam energy density (E_s). The E_s has a direct effect on the phase composition, structure morphology and high-density dislocation. Utu et al. demonstrated that the friction coefficient and wear rate are both determined by the hardness [55], while the hardness is related to the surface structure and dislocations. Due to the characteristic of super-fast heating and cooling speed during the PEBST processing, the microstructure morphology, phase composition and stress distribution, as well as the density of dislocation vary in different conditions. When the E_s is 5 J/cm^2, the surface suffered from the high-temperature cycle. In this condition, the number of subgrains and the value of stress are relatively increased as opposed to the untreated samples. The existence of subgrains and stress contributes to increasing the resistance during the frictional process. Therefore, the wear rate and average friction coefficient both decreased slightly. With the E_s increasing to 10 J/cm^2, the surface layer is still in the "heating mode". There is no melting phenomenon and phase transformation in this condition. The temperature of the surface layer treated by PEBST at 10 J/cm^2 is relatively increased.

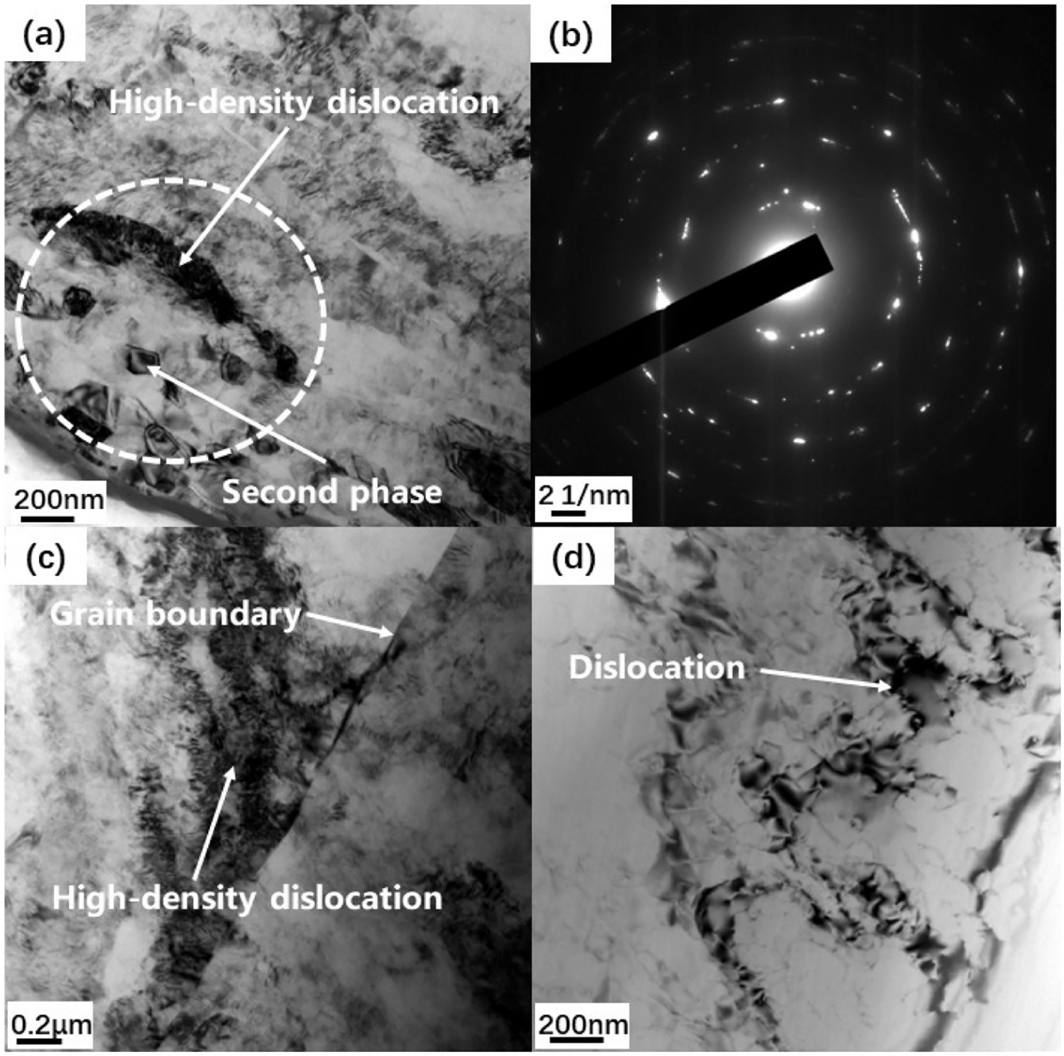

Fig. 8. TEM structure image of additively manufactured Al-Mg alloy after irradiation at $E_s = 5$ J/cm^2: (a) bright field, (b) the SAED pattern of the circular area in (a), (c) the high-density dislocation along grain boundaries, and (d) the dislocation in grains.

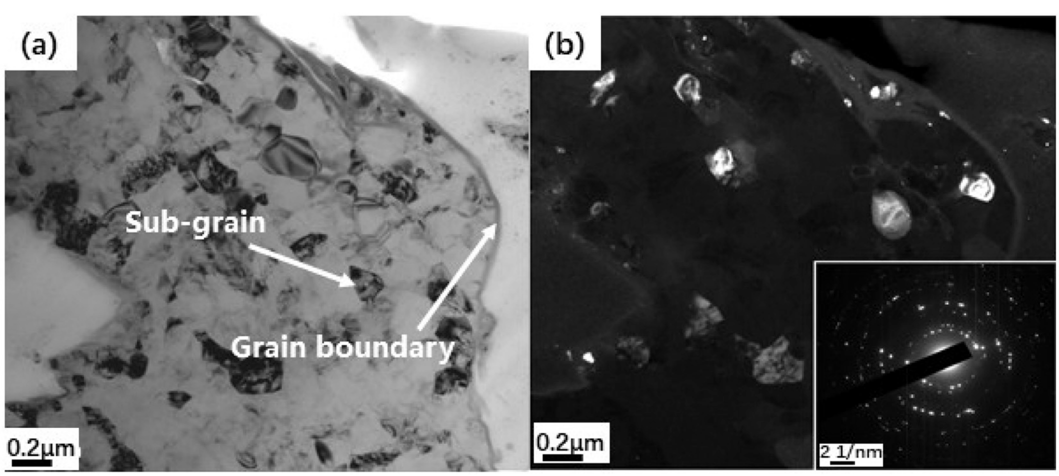

Fig. 9. TEM structure image of additively manufactured Al-Mg alloy after irradiation at $E_s = 10$ J/cm^2: (a) bright-field image, (b) dark-field image and its corresponding SAED pattern [200] Al.

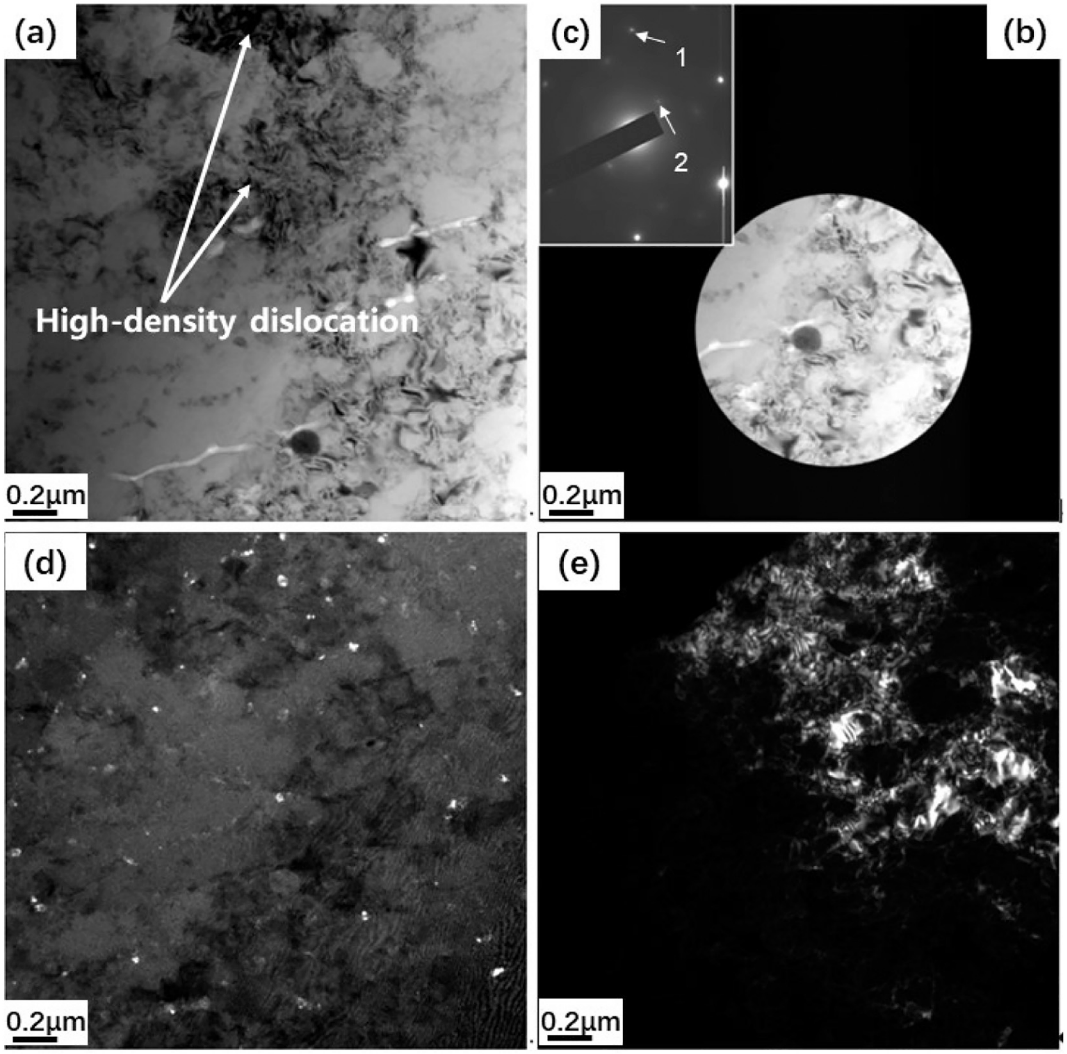

Fig. 10. TEM images of additively manufactured Al-Mg alloys irradiated by electron beam at E_s = 15 J/cm^2: (a) and (b) TEM bright-field images, (c) the SAED pattern obtained from the section of the foil separated by a selector aperture (b) and the arrows indicate the reflections of the dark fields (d)-1 and (e)-2, (d) the dark-field image obtained in the [502] $Mn_{4.6}Fe_{0.4}Si_3$ reflection, (e) the dark-field image obtained in the [420] Al reflection.

The number of subgrains and the value of stress in the modification layer are further increased. The friction resistance gets further strengthened because of the high value of stress distributed in the modification layer and subgrains. Meanwhile, the nano-hardness is improved by the same factors. As the E_s is up to 15 J/cm^2, there is remelted layer and HAZ existed in the modification layer. It is belonging to the "melting mode". Phase transformation and melting phenomena both existed in this condition. The stress distribution in remelted layer and HAZ is different. The modification layer after PEBST at 15 J/cm^2 has complex stress distribution due to the temperature gradient generated in remelted layer and HAZ during the heating and cooling process. Additionally, a number of precipitations (the complex elemental composition $Mn_{4.6}Fe_{0.4}Si_3$) existed in the grains. The complex stress distribution and the formation of precipitations greatly increased the friction resistance. Hence, the wear rate and the average friction coefficient are the lowest among the three PEBST samples.

The hardness and wear resistance of all samples treated in a vacuum chamber without any addition in a short time has been improved. During the PEBST processing, aluminum oxidation is difficult to happen. When the energy density of the electron beam is less than 10 J/cm^2, the dominant factor of the hardness and wear resistance is the stress generated by the high temperature. While the energy density of the electron beam is up to 15 J/cm^2, there are two factors, stress and precipitations, affecting the hardness and wear resistance.

5. Discussion

5.1. *Effects of electron beam energy density on precipitations*

The formation of precipitations is related to the treated temperature of the surface layer. As Fig. 3 shows, the surface temperature of pulsed electron beam treated Al-Mg alloys is increasing with the increase of E_s. When the E_s is 15 J/cm^2, the temperature at the sample surface reaches the aluminum melting point (933 K). While, when the E_s is in the range of 5–10 J/cm^2, the surface temperature of samples is below the aluminum melting temperature. This phenomenon is both appeared in the two duration times (50 μs and 200 μs). Thus, it can be expected that the structural-phase transformation of the aluminum alloy at E_s = 5 or10 J/cm^2 will be carried out within the limits of the solid phase. As for the phase transformation, XRD results in the previous paper demonstrated that when the E_s was less than 10 J/cm^2, the main features of the fraction patterns after irradiation were similar to the one without irradiation and no new phases were detected in this diffractogram [50]. The detected results are consistent with this conclusion. The structural-phase transformations of the alloy at E_s = 15 J/cm^2 will proceed under conditions of high-speed melting and subsequent high-speed crystallization. Fig. 4(d)

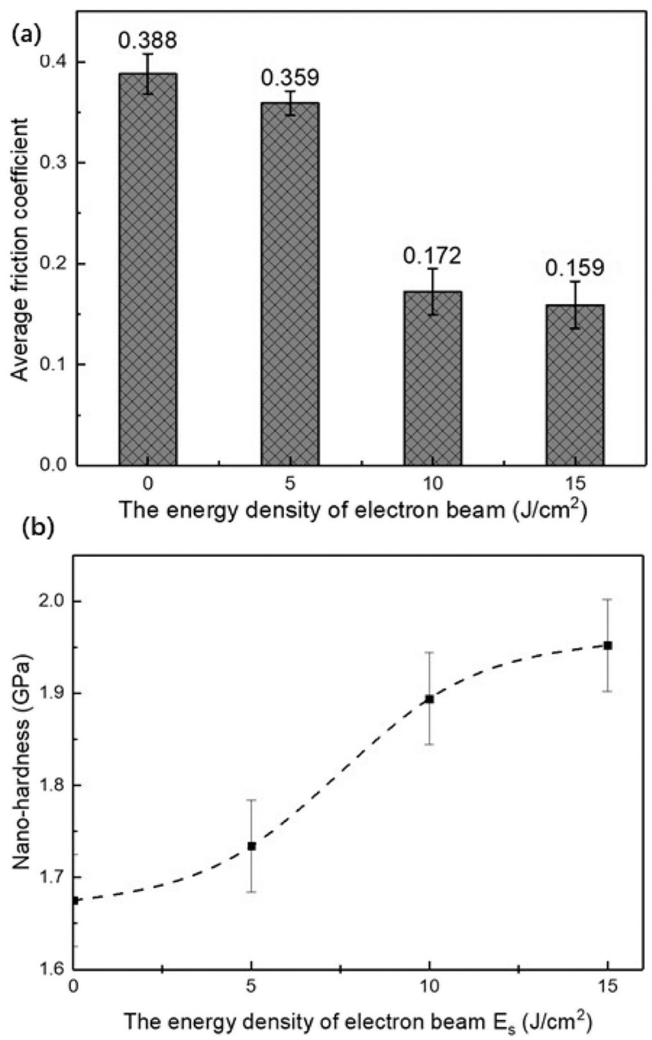

Fig. 11. (a) Average coefficient friction of additively manufactured samples irradiated by different E_s, (b) the surface nano-hardness of Al-Mg specimens irradiated by different E_s.

Table 2
Wear rates of the tested samples in different E_s.

E_s (J/cm^2)	0	5	10	15
Wear rate (10^{-4} mm^3/N/m)	5.23	3.04	0.97	0.75

proves the fact that there is a visible melting layer with the condition at $E_s = 15$ J/cm^2.

The different surface temperatures induced by electron beam irradiation could lead to different effective diffusions. The effective diffusion distance can be written as Eq. (5.1) [56]:

$$\lambda_{eff} = (6Dt)^{1/2} \tag{5.1}$$

where D is the diffusion coefficient and t is the time. The diffusion coefficient is increasing with the increase in temperature [56]. Therefore, When the E_s is less 10 J/cm^2, the atoms have a short effective diffusion distance for forming many precipitations due to less kinetic energy. Based on the analysis of the continuous cooling precipitation diagram of the aluminum alloys [57], superfast cooling speed and short duration time are difficult to generate high kinetic energy, so the formation of precipitations is hindered.

It can be assumed that the formation of precipitations in the surface layer of the alloy is caused by thermal stresses formed in the material during high-speed heat treatment. The thermal stresses generated at the condition of high electron beam energy provide high kinetic energy for atoms moving to form precipitation (solid phase). Quasistatic stress and thermal stress waves dominate the temperature-induced nonstationary thermal stress field. The thermal stress wave is a nonlinear wave with a tiny amplitude of around 0.1 MPa that has a strong impact on the structure and characteristics of materials far beyond the heat-affected zone, as reported in the study [48].

5.2. Relationship between electron beam energy density and dislocation

To quantitatively study the degree of local misorientation under different electron beam irritations, the Eq. (5.2) of average KAM values is adopted [58]:

$$\mathrm{KAMave} = \frac{1}{\mathrm{n}}\sum_{j=1}^{n}\left|\theta_j^{sur} - \theta_i\right| \tag{5.2}$$

where $\mathrm{KAM}_{\mathrm{ave}}$ represents the average value, θ_i is the local misorientation at the point '*i*' and θ_j^{sur} is the misorientation at its neighboring point '*j*'. The local misorientation at a point (283 × 212 nm) was determined according to its all points. The calculated values of $\mathrm{KAM}_{\mathrm{ave}}$, which is got from Eq. (5.2), are shown in Table 3. Local changes in the lattice orientation reflect the lattice curvature which could be used to calculate the geometrically necessary dislocation (GND) density. Due to geometrical restrictions of the crystal lattice, the GND is connected to the strain gradient field and plays a significant role in microstructural length-scale effects on alloy strength [59]. From the KAM value, the average GND density ρ^{GND} can be derived using the following Eq. (5.3) [60]:

$$\rho^{\mathrm{GND}} \approx \frac{\alpha KAM_{ave}}{bu} \tag{5.3}$$

where b is the magnitude of the Burgers vector, u is the distance between the misoriented points(namely the "step size" of the EBSD) and α is a constant dependent on the geometry of the boundaries. In this study, b is set as 0.286 nm for aluminum, u is fixed at 500 nm and α is chosen to be 3 for boundaries of mixed character. The calculated value from Eq. (5.3) is also shown in Table 3. As a result, the value of $\mathrm{KAM}_{\mathrm{ave}}$ and average ρ^{GND} is indeed increasing with the E_s increase. However, the density of dislocation in local areas has few changes when the E_s is increased from 5 to 10 J/cm^2. The quantized dislocation value proves that the low E_s lightly improve the formation of high-density deformation in the irradiated layer. High E_s facilitating the melting phenomenon of the surface layer has a strong effect on the improvement of high-density dislocation.

The analysis of KAM maps with the condition of 5 J/cm^2 irradiation is consistent with the TEM results at the same condition. As seen in Fig. 8 (c) and (d), the low energy density indeed improves the fact of high-density dislocation occurring in the surface layer. As E_s increasing to 10 J/cm^2, there are some second phases (subgrains as seen in Fig. 9(a)) which are also observed in Fig. 5(c) and the KAM values near them are high. In Fig. 10(c), it proves that the formation of the second phase caused by 10 J/cm^2 electron beam irradiation increases the density of dislocation and the stress. When the E_s is up to 15 J/cm^2, the melting phenomenon is visibly seen in Fig. 4(d) and the complex elemental composition $Mn_{4.6}Fe_{0.4}Si_3$ is found in Fig. 10. The areas of high KAM values are increasing due to the formation of the complex elemental composition $Mn_{4.6}Fe_{0.4}Si_3$ which is caused by the irradiation of high

Table 3
The average values of KAM and ρ^{GND} with different E_s.

	E_s (J/cm^2)			
Value	0	5	10	15
$\mathrm{KAM}_{\mathrm{ave}}$ (°)	0.378	0.658	0.697	0.973
Average ρ^{GND} (10^{14} m^{-2})	1.38	2.41	2.55	3.56

electron beam energy (15 J/cm^2), as seen in Fig. 5(d). The size and number of second phases in grains are growing with the high energy density of electron beam irradiation.

There is no melting and phase transformation which corresponds to a so-called "Heating mode" and the surface layer has the melting phenomenon without solid-state phase transformation is considered as the "Meling mode" [25–26]. The deformation and stress state in two modes are different, which was demonstrated by Zhang et al. [49]. It reveals that the stress state in the surface layer is closely bound up with the temperature and energy input. In the "heating mode", the surface layer undergoes compressive stress when the temperature is rising and then tensile stress is generated due to the temperature drop. The distribution of tensile stress in the surface layer depends on the localized stress presented at different depths. As seen in Fig. 5(b) and (c), this stress state is considered to be the tensile stress because of the depths to the surface at room temperature. This phenomenon is similar to the effect of one pulse treatment on the surface layer [49]. When the E_s is up to 15 J/cm^2, the stress state of the melting layer, HAZ zone and substrate is different due to the temperature gradient. The final stress state in the melting and HAZ zones should include residual tensile stress but compressive stress underneath. This can be explained that the high KAM values are found in Fig. 5(d).

6. Conclusions

The experimental evidence and the discussions presented above enable the following main conclusions:

(1) At the condition with lower electron beam energy density (less than 10 J/cm^2), the simulation proved that the surface temperature is below the aluminum melting point. The SEM images show that there is no visible melting layer. With high electron beam energy density (15 J/cm^2), the are melting layer with a size of 30–35 μm and heat-affected zone with a size of around 15 μm which is consistent with the simulation result.
(2) The electron beam energy density facilitates the formation of submicron-crystalline structure and there is no complicated elemental particle distributed in the matrix. When the electron beam energy density increases to 15 J/cm^2, the complex elemental composition $Mn_{4.6}Fe_{0.4}Si_3$ is formed due to the dissolution of submicron-sized inclusions.
(3) The KAM maps reflect the improvement of local misorientation is caused by the electron beam irradiation and the main factor is the formation of high-density dislocation in the irradiated layers. The degree of local misorientation is increased along with the E_s increasing which leads to the increase of stress on the irradiated layer. The KAM value and stress are up to the maximum when the E_s is 15 cm^2. The calculated KAM_{ave} and average ρ^{GND} prove the fact of surface stress and dislocation improved by PEBST.
(4) The electron beam irradiation indeed improves the nano-hardness of additively manufactured Al-Mg alloys. With the electron beam energy density increase, the nano-hardness is increasing and the value of nano-hardness is the highest at the $E_s = 15$ J/cm^2. The rising electron beam energy density is associated with the decreasing friction coefficient and wear rate.

CRediT authorship contribution statement

Conceptualization - Yanfei Geng, Xizhang Chen, Sergey Konovalov, Irina Panchenko;
Investigation, Yanfei Geng, Yurii Ivanov, Vladislav Deev, Evgeny Prusov;
Methodology - Yanfei Geng, Xizhang Chen, Sergey Konovalov, Irina Panchenko, Yurii Ivanov;
Project administration - Sergey Konovalov, Irina Panchenko;
Supervision – Yanfei Geng, Xizhang Chen, Sergey Konovalov, Irina Panchenko, Yurii Ivanov, Vladislav Deev, Evgeny Prusov;
Validation - Yanfei Geng, Xizhang Chen, Sergey Konovalov, Irina Panchenko, Yurii Ivanov, Vladislav Deev, Evgeny Prusov;
Resources - Xizhang Chen, Sergey Konovalov, Irina Panchenko, Yurii Ivanov;
Writing-original draft, all authors;
Review and editing - Yanfei Geng, Xizhang Chen, Sergey Konovalov, Irina Panchenko, Yurii Ivanov, Vladislav Deev, Evgeny Prusov.
All authors have read and agreed to the published version of the manuscript.

Declaration of competing interest

The authors declare that they have no known competing financial interests or personal relationships that could have appeared to influence the work reported in this paper.

Acknowledgments

This project is supported by the Russian Science Foundation (No. 20-79-00194).

Literature

[1] E.L. Huskins, B. Cao, K.T. Ramesh, Strengthening mechanisms in an Al-Mg alloy, Mater. Sci. Eng. A 527 (2010) 1292–1298, https://doi.org/10.1016/j.msea.2009.11.056.
[2] O. Engler, K. Kuhnke, J. Hasenclever, Development of intermetallic particles during solidification and homogenization of two AA 5xxx series Al-Mg alloys with different Mg contents, J. Alloys Compd. 728 (2017) 669–681, https://doi.org/10.1016/j.jallcom.2017.09.060.
[3] J.A. Van Der Hoeven, L. Zhuang, B. Schepers, P. De Smet, J.P. Baekelandt, A new 5xxx series alloy developed for automotive applications, in: SAE Technical Papers, 2002, https://doi.org/10.4271/2002-01-2128.
[4] T. Yuan, Z. Yu, S. Chen, M. Xu, X. Jiang, Loss of elemental Mg during wire+arc additive manufacturing of Al-Mg alloy and its effect on mechanical properties, J. Manuf. Process. 49 (2020) 456–462, https://doi.org/10.1016/j.jmapro.2019.10.033.
[5] W.E. Frazier, Metal additive manufacturing: A review, J. Mater. Eng. Perform. 23 (2014) 1917–1928, https://doi.org/10.1007/s11665-014-0958-z.
[6] C. Su, X. Chen, C. Gao, Y. Wang, Effect of heat input on microstructure and mechanical properties of Al-Mg alloys fabricated by WAAM, Appl. Surf. Sci. 486 (2019) 431–440, https://doi.org/10.1016/j.apsusc.2019.04.255.
[7] A. Horgar, H. Fostervoll, B. Nyhus, X. Ren, M. Eriksson, O.M. Akselsen, Additive manufacturing using WAAM with AA5183 wire, J. Mater. Process. Technol. 259 (2018) 68–74, https://doi.org/10.1016/j.jmatprotec.2018.04.014.
[8] Z. Qi, B. Cong, B. Qi, H. Sun, G. Zhao, J. Ding, Microstructure and mechanical properties of double-wire + arc additively manufactured Al-Cu-Mg alloys, J. Mater. Process. Technol. 255 (2018) 347–353, https://doi.org/10.1016/j.jmatprotec.2017.12.019.
[9] Q. Yang, C. Xia, Y. Deng, X. Li, H. Wang, Microstructure and mechanical properties of AlSi7Mg0.6 aluminum alloy fabricated by wire and arc additive manufacturing based on cold metal transfer (WAAM-CMT), Materials 12 (2019) 2525, https://doi.org/10.3390/ma12162525.
[10] W. Wen, J.G. Morris, An investigation of serrated yielding in 5000 series aluminum alloys, Mater. Sci. Eng. A 354 (2003) 279–285, https://doi.org/10.1016/S0921-5093(03)00017-0.
[11] M.L.C. Lim, J.R. Scully, R.G. Kelly, Intergranular Corrosion penetration in an al-mg alloy as a function of electrochemical and metallurgical conditions, Corrosion 69 (2013) 35–47, https://doi.org/10.5006/0722.
[12] M. Popović, E. Romhanji, Characterization of microstructural changes in an Al-6.8 wt.% Mg alloy by electrical resistivity measurements, Mater. Sci. Eng. A 492 (2008) 460–467, https://doi.org/10.1016/j.msea.2008.04.001.
[13] M.A. Mehedi, K.M.H. Bhadhon, M.N. Haque, Improved wear resistance of Al-Mg alloy with SiC and Al_2O_3 particle reinforcement, JOM 68 (2016) 300–303, https://doi.org/10.1007/s11837-015-1703-2.
[14] J. Xu, W. Liu, Y. Kan, M. Zhong, Microstructure and wear properties of laser cladding Ti-Al-Fe-B coatings on AA2024 aluminum alloy, Mater. Des. 27 (2006) 405–410, https://doi.org/10.1016/j.matdes.2004.11.011.
[15] N. Shaigan, W. Qu, D.G. Ivey, W. Chen, A review of recent progress in coatings, surface modifications and alloy developments for solid oxide fuel cell ferritic stainless steel interconnects, J. Power Sources 195 (2010) 1529–1542, https://doi.org/10.1016/j.jpowsour.2009.09.069.
[16] Y. Fu, J. Hu, X. Shen, Y. Wang, W. Zhao, Surface hardening of 30CrMnSiA steel using continuous electron beam, Nucl. Instrum. Methods Phys. Res., Sect. B 410 (2017) 207–214, https://doi.org/10.1016/j.nimb.2017.08.014.
[17] S. Valkov, M. Ormanova, P. Petrov, Electron-beam surface treatment of metals and alloys: techniques and trends, Metals 10 (2020) 1–20, https://doi.org/10.3390/met10091219.

[18] H. Chouirfa, H. Bouloussa, V. Migonney, C. Falentin-Daudré, Review of titanium surface modification techniques and coatings for antibacterial applications, Acta Biomater. 83 (2019) 37–54, https://doi.org/10.1016/j.actbio.2018.10.036.

[19] V.A. Burdovitsin, E.M. Oks, Fore-vacuum plasma-cathode electron sources, Laser Part. Beams 26 (2008) 619–639, https://doi.org/10.1017/S0263034608000694.

[20] V.A. Burdovitsin, E.S. Dvilis, A.V. Medovnik, E.M. Oks, O.L. Khasanov, Y. G. Yushkov, Surface structure of alumina ceramics during irradiation by a pulsed electron beam, Tech. Phys. 58 (2013) 111–113, https://doi.org/10.1134/S1063784213010039.

[21] Y.F. Ivanov, V.E. Gromov, S.V. Konovalov, D.V. Zagulyaev, E.A. Petrikova, Structural-phase state and the properties of silumin after electron-beam surface treatment, Russ. Metall. (Met.) 2019 (2019) 398–402, https://doi.org/10.1134/S0036029519040189.

[22] D. Zagulyaev, S. Konovalov, V. Gromov, A. Glezer, Y. Ivanov, R. Sundeev, Structure and properties changes of Al-Si alloy treated by pulsed electron beam, Mater. Lett. 229 (2018) 377–380, https://doi.org/10.1016/j.matlet.2018.07.064.

[23] L.X. Song, K.M. Zhang, J.X. Zou, P. Yan, Surface modifications of a hyperperitectic Zn-10wt% Cu alloy by pulsed electron beam treatment, Surf. Coat. Technol. 388 (2020), 125530, https://doi.org/10.1016/j.surfcoat.2020.125530.

[24] R. Franke, I. Haase, M. Klemm, R. Zenker, Friction and wear behaviour of electron beam surface treated aluminium alloys AlSi10Mg(Cu) and AlSi35, Wear 269 (2010) 921–929, https://doi.org/10.1016/j.wear.2010.08.002.

[25] T. Grosdidier, J.X. Zou, B. Bolle, S.Z. Hao, C. Dong, Grain refinement, hardening and metastable phase formation by high current pulsed electron beam (HCPEB) treatment under heating and melting modes, J. Alloys Compd. 504 (2010) S508–S511, https://doi.org/10.1016/j.jallcom.2010.04.010.

[26] T. Grosdidier, J.X. Zou, J. Wu, X.D. Zhang, K.M. Zhang, A.M. Wu, S.Z. Hao, C. Dong, Analysis of metals surface structure modifications induced by high current pulsed electron beam (HCPEB) under the “heating” and “melting” modes, in: Materials Science Forum vol. 614, 2009, pp. 99–104, https://doi.org/10.4028/www.scientific.net/MSF.614.99.

[27] R.G. Song, K. Zhang, G.N. Chen, Electron beam surface treatment. Part II: microstructure evolution of stainless steel and aluminum alloy during electron beam rapid solidification, Vacuum 69 (2003) 517–520, https://doi.org/10.1016/S0042-207X(02)00584-5.

[28] S. Hao, S. Yao, J. Guan, A. Wu, P. Zhong, C. Dong, Surface Treatment of Aluminum by High Current Pulsed Electron Beam q 1, 2001, pp. 203–208, https://doi.org/10.1016/S1567-1739(01)00017-7.

[29] Y. Hao, B. Gao, G.F. Tu, S.W. Li, C. Dong, Z.G. Zhang, Improved wear resistance of Al-15Si alloy with a high current pulsed electron beam treatment, Nucl. Instrum. Methods Phys. Res., Sect. B 269 (2011) 1499–1505, https://doi.org/10.1016/j.nimb.2011.04.010.

[30] Y. Hao, B. Gao, G.F. Tu, Z. Wang, S.Z. Hao, Influence of high current pulsed electron beam (HCPEB) treatment on wear resistance of hypereutectic Al-17.5Si and Al-20Si alloys, Mater. Sci. Forum 675–677 (2011) 693–696, https://doi.org/10.4028/www.scientific.net/MSF.675-677.693.

[31] Q.F. Guan, Q.Y. Zhang, C. Dong, G.T. Zou, Deformation twining in single-crystal aluminum induced by high-current pulsed electron beam, J. Mater. Sci. 40 (2005) 5049–5052, https://doi.org/10.1007/s10853-005-1630-7.

[32] Y. Samih, G. Marcos, N. Stein, N. Allain, E. Fleury, C. Dong, T. Grosdidier, Microstructure modifications and associated hardness and corrosion improvements in the AISI 420 martensitic stainless steel treated by high current pulsed electron beam (HCPEB), Surf. Coat. Technol. 259 (2014) 737–745, https://doi.org/10.1016/j.surfcoat.2014.09.065.

[33] P. Yan, T. Grosdidier, X. Zhang, J. Zou, Formation of large grains by epitaxial and abnormal growth at the surface of pulsed electron beam treated metallic samples, Mater. Des. 159 (2018) 1–10, https://doi.org/10.1016/j.matdes.2018.08.033.

[34] F. Guo, W. Jiang, G. Tang, Z. Xie, H. Dai, E. Wang, Y. Chen, L. Liu, Enhancing anti-wear and anti-corrosion performance of cold spraying aluminum coating by high current pulsed electron beam irradiation, Vacuum 182 (2020), 109772, https://doi.org/10.1016/j.vacuum.2020.109772.

[35] S. Konovalov, D. Zaguliaev, Y. Ivanov, V. Gromov, A. Abaturova, Modification of Al-10Si-2Cu alloy surface by intensive pulsed electron beam, J. Mater. Res. Technol. 9 (2020) 5591–5598, https://doi.org/10.1016/j.jmrt.2020.03.083.

[36] P. Yan, J. Zou, C. Zhang, T. Grosdidier, Surface modifications of a cold rolled 2024 Al alloy by high current pulsed electron beams, Appl. Surf. Sci. 504 (2020), 144382, https://doi.org/10.1016/j.apsusc.2019.144382.

[37] J.X. Zou, T. Grosdidier, B. Bolle, K.M. Zhang, C. Dong, Texture and microstructure at the surface of an AISI D2 steel treated by high current pulsed electron beam, Metall. Mater. Trans. A Phys. Metall. Mater. Sci. 38 (2007) 2061–2071, https://doi.org/10.1007/s11661-007-9146-1.

[38] L. Chai, B. Chen, S. Wang, Z. Zhang, K.L. Murty, Microstructural, textural and hardness evolution of commercially pure Zr surface-treated by high current pulsed electron beam, Appl. Surf. Sci. 390 (2016) 430–434, https://doi.org/10.1016/j.apsusc.2016.08.128.

[39] D.I. Proskurovsky, V.P. Rotshtein, G.E. Ozur, Y.F. Ivanov, A.B. Markov, Physical foundations for surface treatment of materials with low energy, high current electron beams, Surf. Coat. Technol. 125 (2000) 49–56, https://doi.org/10.1016/S0257-8972(99)00604-0.

[40] Y. Liu, K. Zhang, J. Zou, P. Yan, X. Zhang, L. Song, Microstructure and property modifications in surface layers of a Mg-4Sm-2Al-0.5Mn alloy induced by pulsed electron beam treatments, J. Magnes. Alloy 9 (2021) 216–224, https://doi.org/10.1016/j.jma.2020.02.019.

[41] X. Zhang, K. Zhang, J. Zou, P. Yan, L. Song, Y. Liu, Surface microstructure modifications and in-vitro corrosion resistance improvement of a WE43 Mg alloy treated by pulsed electron beams, Vacuum 173 (2020), 109132, https://doi.org/10.1016/j.vacuum.2019.109132.

[42] T.C. Zhang, K.M. Zhang, J.X. Zou, P. Yan, H.Y. Yang, L.X. Song, X. Zhang, Surface microstructure and property modifications in a Mg-8Gd-3Y-0.5Zr magnesium alloy treated by high current pulsed electron beam, J. Alloys Compd. 788 (2019) 231–239, https://doi.org/10.1016/j.jallcom.2019.02.130.

[43] J.J. Fundenberger, B. Beausir, JTEX-Software for Texture Analysis, Université de Lorraine, Metz, France, 2015.

[44] Y. Hao, B. Gao, G.F. Tu, S.W. Li, S.Z. Hao, C. Dong, Surface modification of Al-20Si alloy by high current pulsed electron beam, Appl. Surf. Sci. 257 (2011) 3913–3919, https://doi.org/10.1016/j.apsusc.2010.11.118.

[45] P. Lyu, Y. Chen, Z. Liu, J. Cai, C. Zhang, Y. Jin, Q. Guan, N. Zhao, Surface modification of CrFeCoNiMo high entropy alloy induced by high-current pulsed electron beam, Appl. Surf. Sci. 504 (2020), 144453, https://doi.org/10.1016/j.apsusc.2019.144453.

[46] S. Yang, Z. Guo, L. Zhao, L. Zhao, Q. Guan, Y. Liu, Surface microstructures and high-temperature high-pressure corrosion behavior of N18 zirconium alloy induced by high current pulsed electron beam irradiation, Appl. Surf. Sci. 484 (2019) 453–460, https://doi.org/10.1016/j.apsusc.2019.04.124.

[47] D.I. Proskurovsky, V.P. Rotshtein, G.E. Ozur, A.B. Markov, D.S. Nazarov, V. A. Shulov, Y.F. Ivanov, R.G. Buchheit, Pulsed electron-beam technology for surface modification of metallic materials, J. Vac. Sci. Technol. A 16 (1998) 2480–2488, https://doi.org/10.1116/1.581369.

[48] J. Zou, Y. Qin, C. Dong, X. Wang, A. Wu, S. Hao, Numerical simulation of the thermal-mechanical process of high current pulsed electron beam treatment, J. Vac. Sci. Technol. A 22 (2004) 545–552, https://doi.org/10.1116/1.1697481.

[49] K.M. Zhang, J.X. Zou, B. Bolle, T. Grosdidier, Evolution of residual stress states in surface layers of an AISI D2 steel treated by low energy high current pulsed electron beam, Vacuum 87 (2013) 60–68, https://doi.org/10.1016/j.vacuum.2012.03.061.

[50] Y. Geng, I. Panchenko, S. Konovalov, X. Chen, Y. Ivanov, Effect of electron beam energy densities on the surface morphology and tensile property of additively manufactured Al-Mg alloy, Nucl. Instrum. Methods Phys. Res., Sect. B 498 (2021) 15–22, https://doi.org/10.1016/j.nimb.2021.04.008.

[51] S.I. Wright, M.M. Nowell, D.P. Field, A review of strain analysis using electron backscatter diffraction, Microsc. Microanal. 17 (2011) 316–329, https://doi.org/10.1017/S1431927611000055.

[52] S. Wroński, J. Tarasiuk, B. Bacroix, A. Baczmański, C. Braham, Investigation of plastic deformation heterogeneities in duplex steel by EBSD, Mater. Charact. 73 (2012) 52–60, https://doi.org/10.1016/j.matchar.2012.07.016.

[53] M.N. Gussev, K.J. Leonard, In situ SEM-EBSD analysis of plastic deformation mechanisms in neutron-irradiated austenitic steel, J. Nucl. Mater. 517 (2019) 45–56, https://doi.org/10.1016/j.jnucmat.2019.01.034.

[54] C. Dong, A. Wu, S. Hao, J. Zou, Z. Liu, P. Zhong, A. Zhang, T. Xu, J. Chen, J. Xu, Q. Liu, Z. Zhou, Surface treatment by high current pulsed electron beam, Surf. Coat. Technol. 163–164 (2003) 620–624, https://doi.org/10.1016/S0257-8972(02)00657-6.

[55] I.D. Utu, G. Marginean, Effect of electron beam remelting on the characteristics of HVOF sprayed Al_2O_3-TiO_2 coatings deposited on titanium substrate, Colloids Surf. A Physicochem. Eng. Asp. 526 (2017) 70–75, https://doi.org/10.1016/j.colsurfa.2016.10.034.

[56] X. Sauvage, N. Enikeev, R. Valiev, Y. Nasedkina, M. Murashkin, Atomic-scale analysis of the segregation and precipitation mechanisms in a severely deformed Al-Mg alloy, Acta Mater. 72 (2014) 125–136, https://doi.org/10.1016/j.actamat.2014.03.033.

[57] B. Milkereit, N. Wanderka, C. Schick, O. Kessler, Continuous cooling precipitation diagrams of Al-Mg-Si alloys, Mater. Sci. Eng. A 550 (2012) 87–96, https://doi.org/10.1016/j.msea.2012.04.033.

[58] Z. Yan, D. Wang, X. He, W. Wang, H. Zhang, P. Dong, C. Li, Y. Li, J. Zhou, Z. Liu, L. Sun, Deformation behaviors and cyclic strength assessment of AZ31B magnesium alloy based on steady ratcheting effect, Mater. Sci. Eng. A 723 (2018) 212–220, https://doi.org/10.1016/j.msea.2018.03.023.

[59] J. Zhang, B. Wang, H. Wang, Geometrically necessary dislocations distribution in face-centred cubic alloy with varied grain size, Mater. Charact. 162 (2020), 110205, https://doi.org/10.1016/j.matchar.2020.110205.

[60] Y. Hu, H. Liu, H. Fujii, Improving the mechanical properties of 2219-T6 aluminum alloy joints by ultrasonic vibrations during friction stir welding, J. Mater. Process. Technol. 271 (2019) 75–84, https://doi.org/10.1016/j.jmatprotec.2019.03.013.